Lab on a Chip

PAPER

Characterization of a nanogland for the autotransplantation of human pancreatic islets†

Omaima M. Sabek,‡[ab] Silvia Ferrati,‡[c] Daniel W. Fraga,[a] Juliana Sih,[c] Erika V. Zabre,[c] Daniel H. Fine,[c] Mauro Ferrari,[cdef] A. Osama Gaber[ag] and Alessandro Grattoni*[c]

Despite the clinical success of pancreatic islet transplantation, graft function is frequently lost over time due to islet dispersion, lack of neovascularization, and loss of physiological architecture. To address these problems, islet encapsulation strategies including scaffolds and devices have been developed, which produced encouraging results in preclinical models. However, islet loss from such architectures could represent a significant limitation to clinical use. Here, we developed and characterized a novel islet encapsulation silicon device, the NanoGland, to overcome islet loss, while providing a physiological-like environment for long-term islet viability and revascularization. NanoGlands, microfabricated with a channel size ranging from 3.6 nm to 60 μm, were mathematically modeled to predict the kinetics of the response of encapsulated islets to glucose stimuli, based on different channel sizes, and to rationally select membranes for further testing. The model was validated *in vitro* using static and perifusion testing, during which insulin secretion and functionality were demonstrated for over 30-days. *In vitro* testing also showed 70–83% enhanced islet retention as compared to porous scaffolds, here simulated through a 200 μm channel membrane. Finally, evidence of *in vivo* viability of human islets subcutaneously transplanted within NanoGlands was shown in mice for over 120 days. In this context, mouse endothelial cell infiltration suggesting neovascularization from the host were identified in the retrieved grafts. The NanoGland represents a novel, promising approach for the autotransplantation of human islets.

Introduction

Islet transplantation can improve metabolic control of blood glucose to an extent that has not been possible using injectable insulin,[1] thus offering promising therapy to treat insulin-dependent diabetes mellitus.[1] Despite the success of allotransplantation trials since the introduction of the Edmonton protocol, recent reports have shown that long-term insulin independence is frequently lost by 5 years of follow-up.[2] Conventionally, long-term islet failure is related to loss of islet mass,[3] due to: i) activation of the innate and allogenic immune responses and triggering of thrombogenic pathways in response to islet infusion (the case of allotransplantation),[4] ii) dispersion of islets after infusion in the portal vein,[5] iii) loss of islet viability from lack of neovascularization,[6] and (iv) loss of the physiological pancreatic architecture.

The islet is a complex three-dimensional structure that is organized into an outer mantle of different types of endocrine cells such as α (alpha) – δ (gamma) and Δ (delta) cells clustering around a central core of insulin producing β (beta) cells.[7,8] The islet is integrated spatially around a delicate arterial tree with a complex structure similar to that of a renal glomerulus, which acts as a portal-like system connecting to the pancreatic exocrine venous drainage.[8] The clinical experience makes it evident that for a successful islet transplantation, it is fundamental to re-create the islet physiological microsystems by 1) keeping them in close proximity but separate from each other, 2) supporting the graft with growth factors, 3) promoting rapid revascularization from new, host derived, blood vessels.[9]

Polymeric porous scaffolds,[10] incorporating additional constituents such as extracellular matrix components,[11–14] growth factors,[15] and 'supportive cells' such as fibroblasts[14,16] or stem cells,[13] have been extensively studied for islet transplantation in the extra hepatic, omental pouch, and subcutaneous sites.[10,12,16] Scaffolds are characterized by high

[a]Department of Surgery, The Methodist Hospital, 6565 Fannin Street, Houston, TX 77030, USA
[b]Department of Cell and Molecular biology Weill Cornell Medical College, 1300 York Avenue, New York, NY 10065, USA
[c]Department of Nanomedicine, The Methodist Hospital Research Institute, 6670 Bertner Ave, Houston, TX 77030, USA. E-mail: agrattoni@tmhs.org
[d]Department of Medicine, Weill Cornell Medical College, 1300 York Avenue, New York, NY 10065, USA
[e]Department of Bioengineering, Rice University, 6100 Main Street, Houston, TX 77251, USA
[f]Alliance for NanoHealth, 6670 Bertner Ave, Houston, TX 77030, USA
[g]Department of Surgery, Weill Cornell Medical College, 1300 York Avenue, New York, NY 10065, USA
† Electronic supplementary information (ESI) available. See DOI: 10.1039/c3lc50601k
‡ Equal contribution.

volume to surface ratio, high interconnectivity, and mechanical strength, allowing for 3-dimensional support[17,18] of the islets, mimicking the pancreas architecture. Their pores generally range from 250 to 400 μm,[10,18] which is necessary for the loading of islets in the size range from 50 to 400 μm,[19] and for the rapid diffusion of glucose, insulin, oxygen, nutrients, and vessel formation.

Such a broad pore size distribution, however, leads to loss of small islets (<100 μm) from the scaffold, even at early time points (4 h, *in vitro*).[10] From a clinical perspective, it is fundamental to minimize such loss, since small islets (50–150 nm) have been shown to be superior in terms of insulin secretion and survival rate in both normoxic and hypoxic conditions.[19] This finding suggests that increased retention of small islets should result in a measurable increase in insulin production.

The problem of small islet retention has been investigated by the addition of fibrin gel to post-loaded scaffolds.[10] The gel improved islet retention, but the results failed to detect a statistically significant increase in insulin production. The lack of increased insulin implies that the gel may have affected the islets' response. To avoid the use of additives that may affect the islets' function, we asked if we could use the established microfabrication techniques to rationally design an architecture that could physically minimize the loss of islets while retaining adequate insulin and glucose diffusion. Indeed, previously, microfabrication techniques have been successfully adopted to create devices for immunoisolation of pancreatic islets for allotransplantation.[20–23]

In this study, we focused on the development and characterization of a novel micro- and nanochannel membrane architecture for autotransplantation of islets, the NanoGland. The device is based on a silicon microfabricated membrane designed to host islets in individual 200 μm × 200 μm wells, keeping them in proximity to each other, but separated to prevent islet aggregation. First, a theoretical model was developed to study the effect of different channel sizes on the transport of glucose and insulin in order to determine the optimal NanoGland configurations for the following investigations. Second, NanoGlands were fabricated in 8 different configurations presenting channels from 3 nm up to 60 μm and tested *in vitro* to validate the theoretical model. For this, the islets' function in response to glucose stimuli was assessed during static incubation and perifusion tests. Third, the islets' retention was studied *in vitro* with NanoGlands possessing the most promising configurations (20, 40 and 60 μm), in comparison to 200 μm membranes, which mimicked scaffolds in terms of pore size. Finally, islets loaded into the optimal pre-selected NanoGlands were subcutaneously transplanted in nude mice. Islet viability, glucose stimulated insulin production, and graft vascularization were studied *in vivo* for a period of 120 days.

Experimental details

Membrane architecture and fabrication

Silicon membranes presenting a 6 mm × 6 mm surface area (Fig. 1B) were microfabricated with different channel sizes, including 3.6, 5.7, 13, 20 and 40 nm nanochannels and 20, 40 and 60 μm microchannels. All membranes present a circular pattern of 161 square islet chambers (200 μm × 200 μm, W × H) separated from each other by 50 μm walls (Fig. 1C). Islet chambers are open toward one side of the membrane, while capped by a 30 μm thick silicon layer on the other side. This layer is perforated by arrays of geometrically-defined microchannels etched perpendicularly to the membrane surface, which either connect islet chambers to the outside (in the case
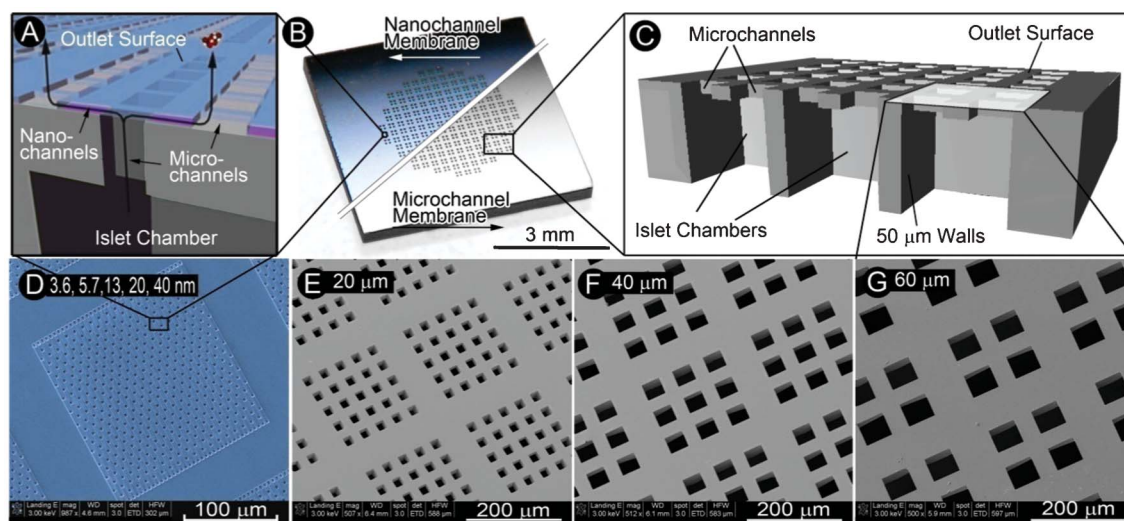

Fig. 1 Silicon membranes: Images of a nanochannel and a microchannel membrane (B); schematic (A) and colored scanning electron microscopy (SEM) micrograph (D) of the nanochannel membrane microstructure; schematic of the microchannel membrane architecture (C) and SEM micrographs showing 20, 40 and 60 μm microchannel arrays (E–G).
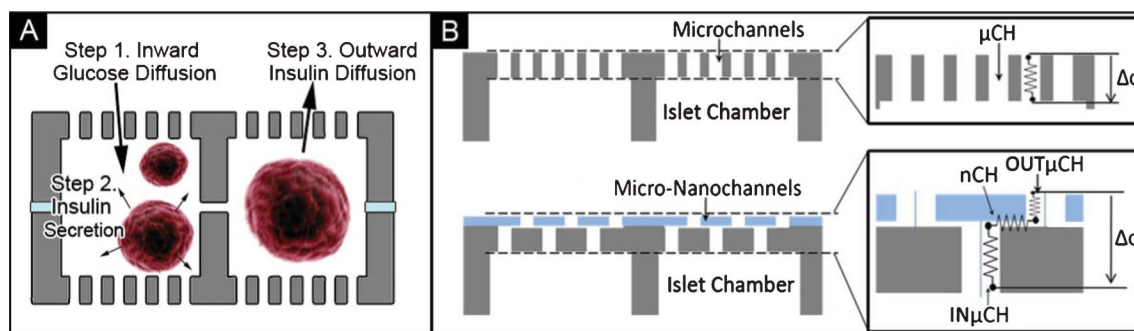
Fig. 2 Schematic of the steps described by the mathematical model (A), schematic of the models employed for micro- and nanochannel membranes (B).

of microchannel membranes, Fig. 1C, E–G) or to nanochannels (Fig. 1A).

Nanochannels, created by a sacrificial layer technique, run parallel to the membrane surface and are connected to the outside by means of a mesh of outlet microchannels (Fig. 1A). Details of the nanochannel microfabrication are available in the literature.[24] The fabrication of the 20, 40, or 60 μm microchannel membranes began by coating both sides of a 500 μm thick four inch silicon wafer with 2.5 μm of SiO_2 by chemical vapor deposition (CVD). One side of the wafer was photolithographically patterned with circular arrays of 161 squares. After transferring the pattern onto the SiO_2 layer using a CHF_3/O_2 dry plasma etch, the oxide was employed as a hard mask, to deep silicon etch (Plasma Therm Versaline) the islet chambers to a depth of 470 μm using the Bosch process. SiO_2 was then stripped in HF and wafers were piranha cleaned. CVD SiO_2 was again deposited ($\sim$600 nm) onto both sides of the wafer. Arrays of 20, 40, and 60 μm squares were then photolithographically patterned onto the unprocessed side of the wafer, aligned to the islet chambers using a Karl Suss MA-6 aligner. The pattern was then transferred into the SiO_2 by a CHF_3/O_2 etch, and deep silicon etched to the bottom of the islet chambers. After stripping the oxide coating in HF a thermal oxidation of the entire wafer surface was finally performed to render the surface homogeneously hydrophilic.

Theoretical model of diffusion

Mathematical description of the membrane

A mathematical model of molecular transport through the micro- and nanochannel membrane of the NanoGland[25] was used (Fig. 2B) to predict the glucose and insulin transfer characteristics, quantifying the delay in insulin-secretion after glucose stimulation for encapsulated islets as compared to free islets. The mathematical simulation was divided into 3 steps: 1) inward transport of glucose, 2) insulin production by the islets in response to the glucose stimuli, taking into account the inward glucose diffusion kinetics through the channels, and 3) the outward transport of insulin (Fig. 2A).

Equivalent resistance to diffusion was calculated for micro- and nanochannel membranes ($R_{\text{equ}\mu\text{CH}}$ and R_{eqnCH}, respectively):

$$R_{\text{equ}\mu\text{CH}} = \frac{1}{n_{\mu\text{CH}}}\left(\frac{L_{\mu\text{CH}}}{D_{\text{A}\mu\text{CH}}A_{\mu\text{CH}}}\right) \quad (1)$$

$$R_{\text{eqnCH}} = \frac{1}{n_{\text{nCH}}}\left(\frac{2L_{\text{IN}\mu\text{CH}}}{D_{\text{A}\mu\text{CH}}A_{\text{IN}\mu\text{CH}}} + \frac{L_{\text{nCH}}}{D_{\text{nCH}}A_{\text{nCH}}} + \frac{2L_{\text{OUT}\mu\text{CH}}}{D_{\text{A}\mu\text{CH}}A_{\text{OUT}\mu\text{CH}}}\right) \quad (2)$$

where $n_{\mu\text{CH}}$, $L_{\mu\text{CH}}$ and $A_{\mu\text{CH}}$ represent the number, length and cross-sectional area of the microchannels. In eqn (2), n_{nCH} is the number of nanochannels, $L_{\text{IN}\mu\text{CH}}$, L_{nCH}, $L_{\text{OUT}\mu\text{CH}}$ and $A_{\text{IN}\mu\text{CH}}$, A_{nCH}, $A_{\text{OUT}\mu\text{CH}}$ represent the length and cross-sectional area of the inlet microchannel, the nanochannel and the outlet microchannel, respectively (see Table 1). D_{nCH} and $D_{\text{A}\mu\text{CH}}$ are the scaled diffusivity and apparent diffusivity at the nano- and microscale, respectively. At the nanoscale, concentration-driven transport is dominated by diffusion and scaled D_{nCH} can be obtained for each nanochannel size according to Deen's hindrance theory.[26] In the case of microchannels, the fluid transport is likely to be affected by convective flows. Thus, $D_{\text{A}\mu\text{CH}}$ cannot simply be considered equal to the bulk diffusivity, but it needs to account for convection through a factor, δ, which depends on the size of microchannels. The derivation of D_{nCH} and $D_{\text{A}\mu\text{CH}}$ is detailed in the following paragraph. The cumulative mass release [$m(t)$] was obtained for both glucose and insulin as:

$$m(t) = V_{\text{OUT}}c(t) = (C_{\text{IN}} - C_{\text{OUT}})\frac{V_{\text{IN}}V_{\text{OUT}}}{V_{\text{IN}} + V_{\text{OUT}}}(1 - e^{-\tau t}) \quad (3)$$

$$\tau = \left(\frac{1}{R_{\text{eq}}V_{\text{IN}}}\right)\left(1 + \frac{V_{\text{IN}}}{V_{\text{OUT}}}\right) \quad (4)$$

where C_{IN} and C_{OUT} are inlet and outlet concentrations at time 0, and V_{IN} and V_{OUT} are the volumes of the source and sink reservoirs, respectively, and R_{eq} relates to either of the micro- or nanochannel membranes.

Diffusivity scaling in micro- and nanochannels and convective factor

The diffusion of analytes through nanochannels is dominated by physical confinement and electrostatic interactions between molecules and channel walls, determining deviation with respect to continuum conditions. Diffusivity scaling was

Paper

Table 1 Characteristic size and numbers of channels in the micro- and nanochannel membranes. Units are in µm unless otherwise specified

| | Microchannel Membrane | | | |
	Width (µm)	Length (µm)	Depth (µm)	Number of channels per membrane
Islet chamber	200	200	470	161
20 µm microchannels	20	20	30	4025
40 µm microchannels	40	40	30	1449
60 µm microchannels	60	60	30	644
	Nanochannel Membrane			
	Width (µm)	Length (µm)	Depth (µm)	Number of channels per membrane
Islet chamber	200	200	670	161
Inlet microchannels	3	30	2	156 975
Outlet microchannels	3	1.7	3	163 254
Nanochannels	3	1	3.6, 5.7, 13, 20, 40 nm	313 950

considered for glucose and insulin and calculated according to Deen's hindrance theory[26] (table in Fig. 3):

$$D = HD_{bulk} \quad (5)$$

$$H = (1 - \lambda)(1 - 1.004\lambda + 0.418\lambda^3 + 0.21\lambda^4 - 0.169\lambda^5) \quad (6)$$

where H is the hindrance factor for sphere-like molecules in *slit*-channels and λ is the molecule's hydrodynamic diameter to channel size ratio. For glucose, a hydrodynamic radius r_h equal to 3.9 Å was considered, accounting for the Stuart and Briegleb correction[27] to the Stokes–Einstein value, required when solute and solvent present comparable molecular volumes. For insulin $r_h = 2.86$ nm was adopted,[28] accounting for its hexameric quaternary structure at physiological conditions (pH 7).[29] Low concentrations of analytes were adopted experimentally. As such, bulk diffusivities of 6.75×10^{-6} and 1.14×10^{-6} cm^2 s^{-1} were considered for glucose and insulin hexamers, respectively, disregarding the dependence on concentration (details in the ESI†). To evaluate the extent of influence of convective transport on fluid transport across our micro- and nanochannel membranes, glucose diffusion

experiments were performed with 40 nm, and 20, 40 and 60 µm membranes (details in ESI†, section 2). Additionally, our previously published data of glucose diffusion across 5.7 nm channels were also used.[30] By fitting the experimental data with eqn (3) and eqn (4), apparent diffusivity values (D_A) were obtained. A convective factor, $\delta = D_A/D$, was then computed (see table in Fig. 3). As expected, δ was $\cong 1$ for the nanoscale channels, and δ was found to increase proportionally to the cube of the channel size (Fig. 3B). This is in good agreement with convective mass transport laws,[31] where mass release rate (m) is proportional to h^3, where h is the characteristic channel size. Finally, for nanochannels D values obtained through Deen's hindrance theory were finally used. For microchannels, $D_A = \delta D$ was employed.

The increase in glucose concentration, $c_G(t)$, within the NanoGland, following an external glucose stimulation of 4000 µg mL^{-1}, was calculated for each channel size. To employ a realistic, biphasic insulin secretion rate profile as a function of glucose stimulation, experimental data of a static stimulation of free islets were fitted with the mathematical expression:
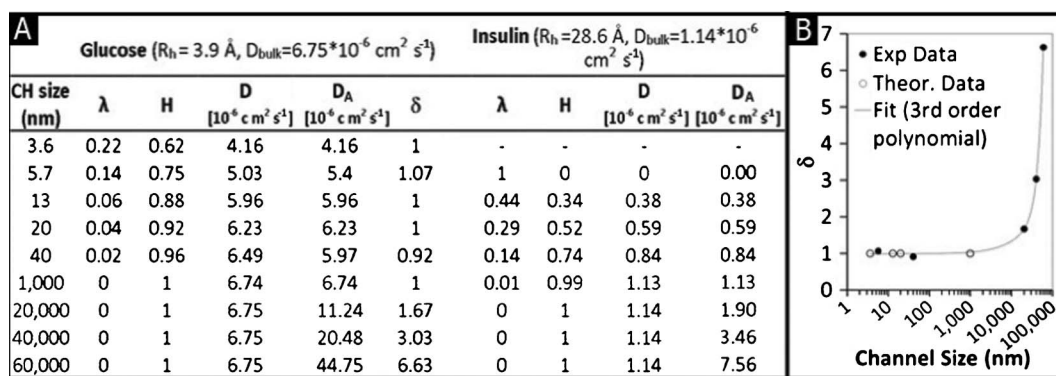

Fig. 3 Hindrance and convective factors (H and δ respectively), scaled diffusivity (D) and apparent diffusivity (D_A) values obtained for glucose and insulin hexamers at 37 °C as a function of the channel size, (A); graph showing the profile of δ as a function of the channel size, (B). The graph displays both the obtained experimental data as well as the theoretical values based on Deen's hindrance theory.

$$\dot{m}_{s}(t) = A_1(e^{-A_2 t} - e^{-A_3 t}) + A_4 \frac{e^{-\frac{(t-A_5)^2}{2A_6^2}}}{\sqrt{2\pi}A_6} \qquad (7)$$

where $A_{1 \text{ to } 6}$ are fitting coefficients. By integrating eqn (7) the cumulative insulin release was obtained as:

$$m_{s}(t) = A_1\left(\frac{e^{-A_3 t}}{A_3} - \frac{e^{-A_2 t}}{A_2}\right) + \frac{A_4}{2}\left[1 + erf\left(\frac{t-A_5}{A_6\sqrt{2}}\right)\right] + c \qquad (8)$$

where c is a constant. Details of the experimental analysis and the mathematical fitting are reported below and in the ESI,† respectively. Islets secrete insulin proportionally to the glucose stimulation. The secretion characteristic $I(c_G)$, as a function of glucose concentration has been well characterized by Harrison *et al.* with human islets[32] (ESI† Section 1). Following a sudden external glucose stimulation, the rate of increase in glucose concentration within a NanoGland proportionally depends on the size of the channels. As a consequence, islets contained within microchannel NanoGlands will secrete insulin at a higher rate as compared to the case of nanochannel NanoGlands. To take this into account, and to obtain the insulin release profile for encapsulated islets, the insulin release profile of free islets, eqn (7), was scaled-down according to the glucose concentration reached in each NanoGland at 30 s after stimulation. This time was selected based on the cellular insulin secretion delay described by Stamper and Wang[33] The resulting insulin secretion rate from islets encapsulated in the NanoGland, $\dot{m}_{IP}(t)$, was obtained as $\dot{m}_{IP}(t) = \alpha\dot{m}_{s}(t)$, where $\alpha = I(c_{G,t=30s,\text{NanoGland}})/I(c_{G,t=30s,\text{free islets}})$. At each time, the insulin release from the NanoGland is determined by the concentration of insulin within the NanoGland, $c_I(t)$, which in turn depends on insulin produced, m_{IP}, and insulin released, m_{IR}:

$$\frac{dc_I}{dt} = \frac{1}{V}\frac{dm_{IP}}{dt} - \frac{1}{V}\frac{dm_{IR}}{dt} \qquad (9)$$

$$m_{IR}(t) = \varepsilon c_I(t) \qquad (10)$$

where the proportionality factor ε is calculated based on eqn (3) and eqn (4) for each channel size (see ESI† Section 1).

Testing devices and the NanoGland

For the *in vitro* viability study, membranes were assembled into polystyrene cell culture inserts (Becton Dickinson, USA) by replacing the polymeric membrane of the insert with a silicon membrane presenting islet chambers facing upward (Fig. 4A). The membrane was glued in place using biocompatible EPO-TEK® 353ND epoxy (10 : 1 Part A : Part B ratio), which was hardened on a hot plate (120 °C, 60 s) and completely cured in an oven (110 °C, 30 mins).

For the *in vitro* perifusion study and the *in vivo* analysis, two identical membranes, separated by medical-grade spacing rings (Apple Rubber, Lancaster, NY, USA), were assembled into NanoGlands with islet chambers facing inward (Fig. 4B). The components were glued and sealed using an implantable-grade silicone adhesive (MED2-4213, NuSil Silicone Technology, CA). After applying extra silicone adhesive to smooth the sharp edges of membranes, NanoGlands were cured in the oven (150 °C for 15 mins) and sterilized by immersion in ethanol. After sealing, islets were loaded into the NanoGland by means of a micropipette laterally inserted through the self-sealing silicone adhesive. A schematic of the NanoGlands assembly is reported in ESI† Fig. S4. Fig. 4C shows an SEM image of a human pancreatic islet sitting on the surface on a nanochannel membrane.

Human pancreatic islets

Human pancreata were obtained from brain dead heart-beating donors with informed consent for transplant or research. Islets were isolated using our standard technique[34–36] (additional references in ESI† Section 2). Aliquots of isolated human islets were cultured in Memphis Serum-Free Medium (*M*-SFM) further supplemented with 10 U mL^{-1} heparin and 10 mM Niacin as previously described.[34,35,37] During the culture period, culture media were replaced at day 1 post-isolation and thereafter based on relative islet purity according to established protocols.[35,37]
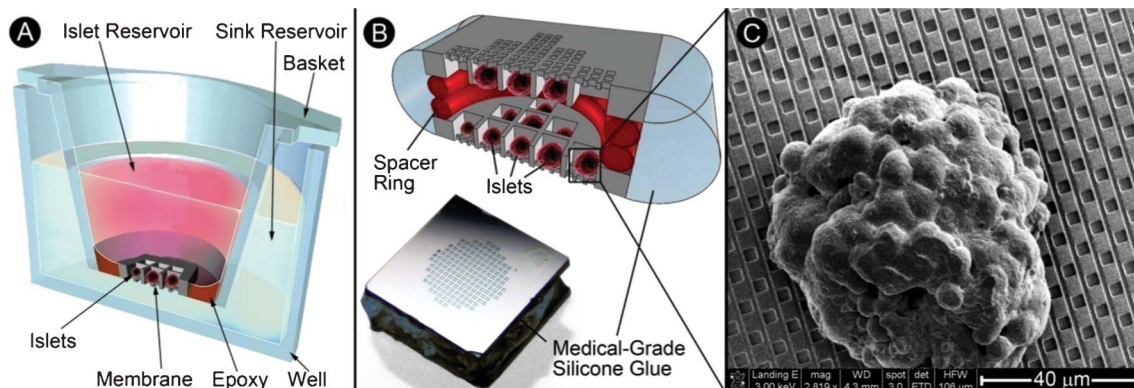

Fig. 4 Schematic of the insert-well setup used *in vitro* for the static islet viability test (A); picture and schematic of the membrane capsule-assembly adopted for the *in vitro* islet viability testing during continuous perifusion and *in vivo* analysis (B); SEM micrograph of a pancreatic islet sitting on the surface of a nanochannel islet chamber (C).

Assessment of human islets' function *in vitro*

Insulin secretion in response to glucose challenge was tested by static incubation and perifusion. Two static incubation experiments were performed. *Experiment 1* (*short-term*): 100 islets equivalent (IEQ, the standard estimate of isolated islet volume) were tested either free or loaded into NanoGlands (20, 40, 60 μm, and 40 nm). Free or encapsulated islets were first immersed in 3 mL of low-glucose medium (30 mg dL^{-1}, basal) for 60 mins and then challenged with 3 mL high-glucose medium (400 mg dL^{-1}) for an additional 120 mins. 500 μL samples of supernatant were collected at 1, 2, 3, 4, 5, 7.5, 10, 20, 30, 45, 60, 90, and 120 mins. After each sampling an equivalent amount of fresh high glucose medium was reintroduced to maintain constant supernatant volume. Samples were measured for insulin content using an ELISA assay (Alpco Diagnostics, Windham, NH). Data were collected and normalized to take into account the fluid dilution occurring at each sampling.

Experiment 2 (*long-term*): Standard aliquots of 50–100 islets equivalent were cultured, either free or loaded in cell culture inserts (20, 40, 60 μm) for 30 days. At days 5 and 27, islets were first treated with low-glucose medium (30 mg dL^{-1}, basal) for 60 mins and then challenged with high-glucose medium (400 mg dL^{-1}) for an additional 60 mins. Media samples were collected at 60 and 120 mins and measured for insulin content using the same ELISA assay as above. The stimulation index (SI) was calculated by dividing insulin released per IEQ during the stimulation period with high-glucose medium (400 mg dL^{-1}) by the insulin released during the basal period (30 mg dL^{-1}). At the end of both experiments (day 30), islets were harvested, fixed in formalin for 24 h, and processed for either confocal or histological analysis of insulin staining (see sections below).

Perifusion method: 83 IEQ either free or loaded into NanoGlands (20, 40, 60 μm, and 40 nm) were inserted into a perifusion apparatus (ESI† Fig. S5) and primed with low-glucose medium (30 mg dL^{-1}). All perifusion capsules were then subjected to a constant flow (1.0 mL min^{-1}) of low-glucose solution at 37 °C for one hour, followed by high-glucose solution (400 mg dL^{-1}) for two hours. Finally, the medium was returned to low-glucose for an additional 40 mins. During the procedure, samples of the effluent medium were collected at 40, 50 and 60 mins during the low-glucose phase, then each minute for the first 10 mins of high-glucose then at several intermediate time points until 160 mins. Samples were analyzed for insulin release by means of an ELISA assay (Alpco Diagnostics, Windham, NH).

NanoGland islet retention

The size distribution of the human islets was evaluated by optical microscopy (Olympus IX71) and data analysis employing two image software programs (Adobe Photoshop CS2 and ImageJ software). 30 islet images were acquired from different clinical samples collected over 5 years. The outline of each islet was manually selected with the help of Photoshop and the sizes were automatically computed by ImageJ. Islets are routinely counted based on size ranging from 50 μm to greater than 350 μm, but, for the purpose of our study, islets less than 50 μm in size were also counted.

The ability of NanoGlands presenting different channel sizes (20, 40, 60, and 200 μm) to retain the encapsulated islets was tested by employing the insert-well set up previously shown in Fig. 4 A. Prior to loading into the baskets, 4 separate islet aliquots were characterized in terms of size and number. Each aliquot was re-suspended into 800 μL of culture medium and then loaded into their respective inserts (150–500 IEQ per insert), ensuring complete transfer of islet tissue. The microplate was placed on a Labnet Orbit P4 orbital shaker set to 300 rpm and allowed to gently agitate for 24 h. After the incubation was complete, the baskets were removed from the wells and the islet tissue that had passed through the channel membranes was counted and sized.

Subcutaneous transplantation of human islets using Nanoglands

A short- and a long-term *in vivo* experiment were performed over 30 and 120 days, respectively. For both experiments human islets were prepared as follows. After 72 h in culture, the islets were tested to determine *in vitro* viability and suitability for transplantation based on standardized criteria employed for clinical human use (stimulation index >1.0; viability >70%; purity >30%; no bacterial or fungal contamination). The islet preparations used in the experiment fully satisfied the clinical criteria. Animals were housed and treated in accordance with the policies and procedures of the Animal Welfare Committee with all testing performed using IACUC-approved protocols at The Methodist Hospital Research Institute.

30-days assessment of human islets function *in vivo*

Human islets were loaded into 20, 40 or 60 μm NanoGlands (approximately 350 IEQ/NanoGland, 15 NanoGlands/channel size) and transplanted subcutaneously in non-diabetic immuno-deficient mice (nude) ($n = 5$, 3 implants per animal, 15 animals total). Equivalent aliquots of human islets (1000IEQ) were transplanted free under the left kidney capsule as a control ($n = 5$). At day 7 and 14 post-transplantation, mice were weighed and injected intraperitoneally with glucose (2 g per kg of body weight), following an overnight fast. Thirty mins after glucose injection, blood samples were collected to quantify human insulin in the plasma using an ELISA assay (Alpco Diagnostics) which has negligible cross-reactivity to mouse insulin (<1.0%) (ESI† Section 3).

120-days vascularization analysis

Islets were loaded into 20, 40 or 60 μm NanoGlands (approximately 350 IEQ/NanoGland) and implanted subcutaneously into 3 mice (3 implants per mouse). In parallel, five control animals received islets under the renal capsule. After 120 days, animals were tested for insulin secretion at 60 and 90 mins post-glucose challenge, as described above. Human insulin levels in blood were determined by an Ultrasensitive ELISA assay (Mercodia Diagnostics, Uppsala, Sweden). The ultrasensitive assay has less than 0.3% cross reactivity with mouse insulin and a lower detection limit of 0.15 μU mL^{-1}. Animals were then euthanized and the NanoGlands and

surrounding tissues were harvested and fixed in formalin for 24 h.

Confocal microscopy

Islets were retrieved from NanoGlands, embedded in agarose gel and then in paraffin. 5 μm sections of the recovered islets were mounted on slides, dewaxed and antigen retrieval was carried out with citrate buffer at low-power in a microwave. Islets were then stained for immunofluorescent analysis using rabbit anti-human insulin (mAb #3014, Cell Signaling Technologies, MA, USA) followed by Alexa Fluor® 594 goat anti-rabbit (A11012, Life Technologies, NY, USA). The control sample was treated only with the secondary antibody to assess unspecific staining. Slides were then imaged with a Nikon Eclipse confocal microscope equipped with a 60× objective.

Histological analysis

Masson's Trichrome staining was performed on the tissues surrounding the NanoGlands to assess collagen content. NanoGlands bearing islets were stained for human insulin and glucagon employing a primary antibody (Ab7842, Abcam, MA, USA) and a polyclonal Rabbit Anti-Human Glucagon (cat# A0565, Dako, CA, USA), respectively, followed by horseradish peroxidase-conjugated secondary antibody and DAB staining. Staining for capillary endothelial cells was performed using a CD34 primary antibody (clone MEC14.7 Cat No: GTX28158; GeneTex Inc., CA, USA) or a rat anti-mouse CD31 antibody (Clone MEC 13.3 Cat# 553371 BD Pharmingen, CA, USA), followed by streptavidin phosphatase. To assess islet viability, we employed Tunnel Stain kit S-7100 (Millipore). The staining was performed according to the manufacture's protocol, developing the samples in DAB for 3 min. Counter-staining was performed in Mayer's Hematoxylin for 1 min. NanoGlands were then imaged with an Olympus BX51 optical microscope

equipped with a 100× objective. Due to the loss of islets upon NanoGlands disassembly, only a qualitative evaluation of the staining was possible.

Results and discussion

Theoretical model

A mathematical description of a 21 μL NanoGland immersed in infinite sink conditions was developed to study the response kinetics of encapsulated islets following a glucose stimulus. The model was used to compare NanoGlands possessing different channel sizes to select the best configuration for further *in vitro* and *in vivo* testing. The mathematical simulation was divided into 3 steps: 1) inward transport of glucose, 2) the islets' insulin production in response to the glucose stimuli within the NanoGland, and 3) the outward transport of insulin (Fig. 2A). In the first step, the increase in glucose concentration within the NanoGland was computed by setting the sink solution to a glucose concentration of 4 mg mL^{-1}. The theoretical results are shown in Fig. 5A in comparison to experimental curves. The results distinctly showed that the kinetics of transport through the NanoGland membranes was determined by the channel size and cross sectional area. In this context, good agreement was found with experimental curves. In 3.6 and 5.7 nm nanochannels, the physical confinement produced a reduction in glucose diffusivity by approximately 40% and 25% respectively as compared to the bulk value of 6.75 × 10^{-6} cm^2 s^{-1}. This, in combination with a limited active membrane cross-section, would cause a very slow increase in glucose concentration within the NanoGlands. A different scenario was instead shown for large microchannels (60 and 40 μm), where the transport of glucose is not only determined by diffusion, but
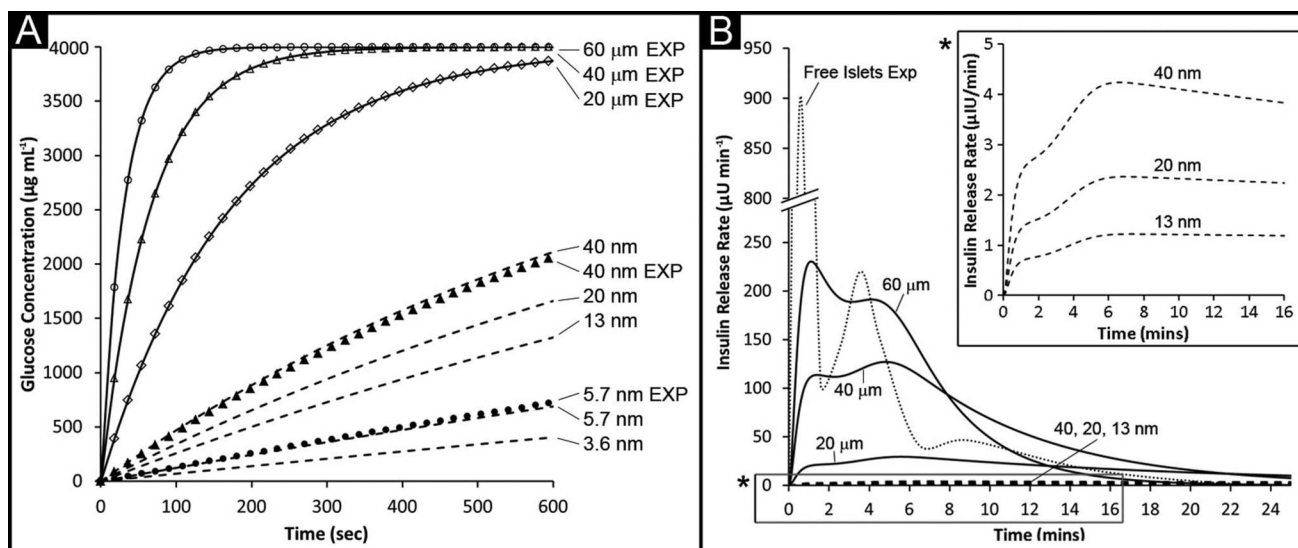

Fig. 5 Theoretical model of glucose and insulin diffusion through different micro- and nanochannels for selection of appropriate membranes. (A) Theoretical profiles of inward glucose transport into the NanoGland, following an external glucose stimulation of 4 mg mL^{-1} as compared to experimental results; (B) simulated cumulative insulin release from the NanoGlands. A conversion factor of 45.5 μg U^{-1} was considered in the calculation. Experimental results of insulin secretion rate from free islets during static stimulation are also shown.

also enhanced by convective flows associated to the experimental conditions, including differences in fluid density and fluid mixing. Experimental results of glucose release from 20, 40 and 60 μm microchannel membranes (see ESI† section 2) have indeed shown a glucose transport consistent with apparent diffusivities $D_A > D_{bulk}$, which increase at increasing channel size and which determine a rapid inward transport of glucose. Based on the proposed model, at the representative time of 30 s, glucose reached values of 21 and 2511 μg mL^{-1} for the 3.6 nm and 60 μm NanoGlands, respectively.

For the second step, insulin secretion from islets contained in the NanoGland was calculated by scaling the biphasic secretion profile of the free islets during static stimulation. This was done according to the glucose concentration reached in each NanoGland at 30 s after stimulation and the sigmoidal secretion characteristics described by Harrison et al. (ESI† Fig. S2). A secretion-limiting effect of insulin accumulation within the NanoGland was neglected. Pancreatic β-cells express insulin receptors,[38] which could potentially activate a negative feedback, regulating insulin release. Numerous in vitro and in vivo studies have been conducted to investigate this aspect, however contrasting results have been presented indicating either no effect[39] or a suppressive effect[40] of exogenous insulin on insulin secretion. Recently, Anderwald et al.[41] showed that the insulin release can in fact be modulated by exogenous insulin, but this depends on whole-body insulin sensitivity. Specifically, in highly sensitive subjects, insulin increases its own secretion, while it exerts a suppressive effect in insulin-resistant and type 2 diabetic subjects. Because of the lack of solid experimental conclusions and the complexity of this biofeedback mechanism, our model disregarded any stimulating or suppressive effect of accumulated insulin in the NanoGlands on insulin secretion.

In the third and final step of simulation, the release profile of insulin from the NanoGland was calculated (Fig. 5B). It is to be noted that, due to its molecular size, the insulin hexamer cannot diffuse through either 3.6 or 5.7 nm nanochannels, the latter of which corresponds to the molecule's hydrodynamic diameter.[28] The differences observed in glucose diffusion profiles from different channel sizes are accentuated in the case of insulin. Indeed, the extent of physical and electrostatic confinement on diffusing insulin was significant and produced a 67% reduction in its diffusion coefficients with respect to the bulk value (the case of 13 nm). The model prediction maintains the biphasic profiles of insulin release as experimentally observed for free islets. However, at decreasing channel size, the early time point peak (measured at 1 min for free islets) becomes lower in intensity while the overall profile becomes smoother and extends for longer time points. This is due to the dampening effect of the membranes, which limits the amount of insulin released regardless of the insulin secreted.

The results from our model indicate that microchannel NanoGlands may represent the only valuable option providing sufficiently rapid insulin response to glucose stimuli. In light of this, for further in vitro and in vivo testing we primarily focused on microchannel NanoGlands.

Assessment of human islets' function in vitro

The preservation of encapsulated human islets' function in response to glucose stimuli was examined by measuring the islets insulin secretion in response to glucose challenge using static incubation (short- and long-term experiments, Fig. 6) and perifusion methods (Fig. 7). The results were compared with the simulated insulin release profiles obtained with the mathematical model. Insulin storage in the islet β-cells was also tested using insulin staining (Fig. 6D–F).

Static stimulation testing

Experiment 1: Cumulative release results for encapsulated islets (60, 40, 20 μm, and 40 nm) show a similar insulin secretion profile to free islets (Fig. 6A). However, as expected, the extent of insulin secreted proportionally diminishes at decreasing channel sizes. For all profiles, an early rapid increase in insulin released is observed, followed by an exponential-like tapering off after approximately 10 mins. This is more clearly displayed in the release rate graph (Fig. 6B) where a spike of insulin at 1 min post-glucose challenge is shown for all experimental groups. Despite the variability in experimental data, a biphasic secretion is noticeable for all NanoGland configurations, which is more evident for the microchannel devices. Although the model predictions tend to underestimate the insulin release, especially for smaller channels, experimental (Fig. 6B) and theoretical results (Fig. 5B) are in good agreement and provide a general validation for the use of the model for the selection of NanoGlands.

Experiment 2: In order to assess the long-term function in vitro, islets were cultured, either free or loaded in NanoGlands (20, 40 and 60 μm), for 30 days and were challenged with glucose at day 5 and 27. Fig. 6C shows that encapsulated human islets had a stimulation index (SI) greater than 1.0, a sign of functional islets. A general decrease in insulin SI was observed at day 27 compared to day 5 in all cases, including free islets. This may be related to the loss of function due to the extended period in culture, consistent with literature data.[17] Islets loaded into 60 μm membranes and cultured for 30 days were also analyzed by histology and immunofluorescence staining for human insulin. The histological (Fig. 6D) and confocal (Fig. 6E and F) images show positive insulin staining suggesting that the islets' function was preserved.

Perifusion stimulation testing

Fig. 7 shows the dynamic insulin release profile in response to glucose for free and encapsulated islets (60, 40, 20 μm and 40 nm NanoGlands). Similar profiles as compared to those obtained from the theoretical prediction (Fig. 5B) and the static experiment 1 (Fig. 6A and B) were obtained for all the experimental groups. A characteristic insulin spike at 1 min post-glucose challenge was accompanied in this case by a steady level of insulin release maintained over the following 10 mins. As for the static stimulation, insulin levels were observed to depend on the size of channels of the NanoGland. However, lower differences between free and encapsulated islets were noticed, which could be due to the compensation effect of convective flows during perifusion.
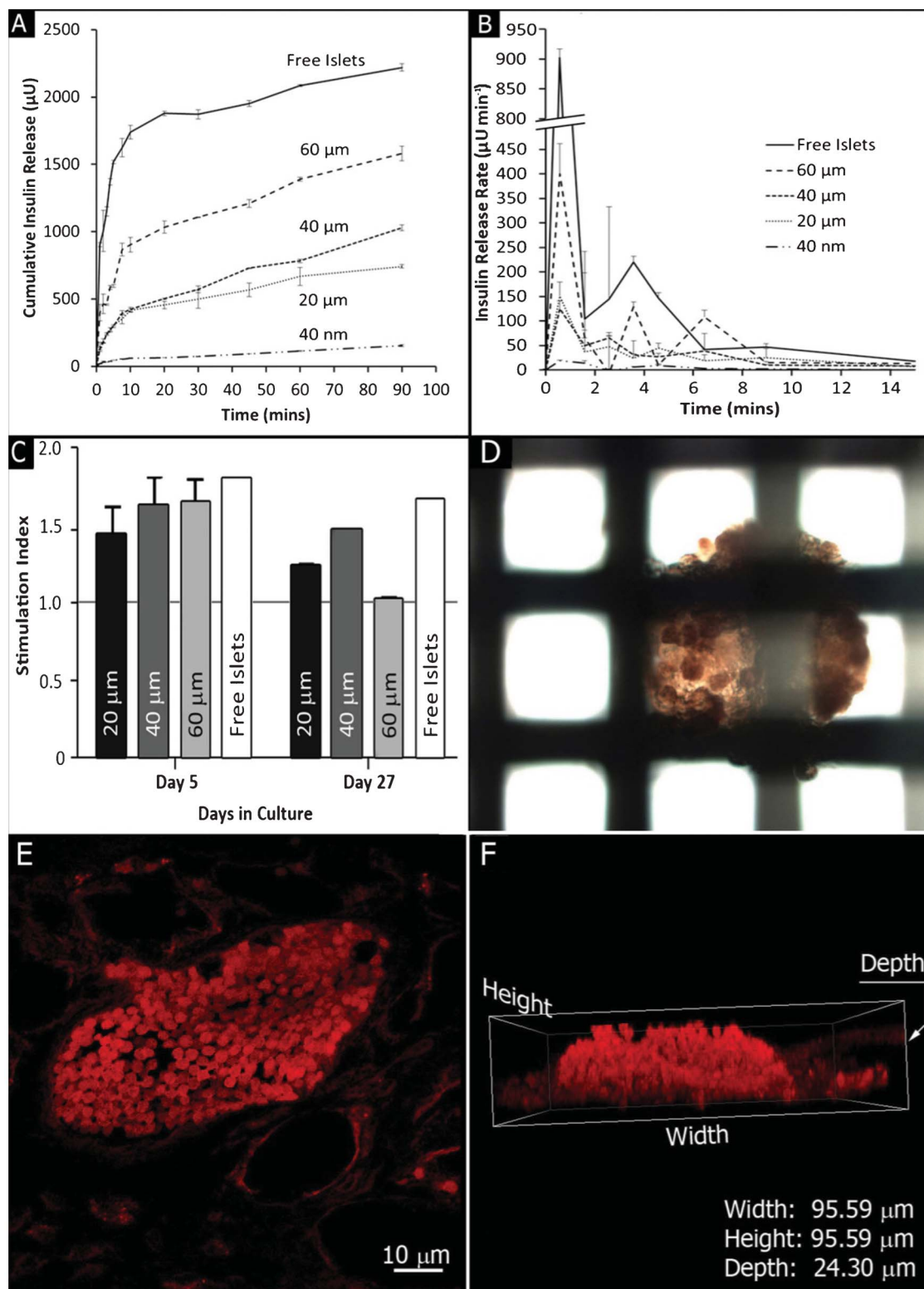
Fig. 6 *In vitro* static testing of NanoGland-encapsulated islets (50–100 IEQ) stimulated by glucose: (A) Cumulative insulin release and (B) insulin release rate obtained during short-term static experiments with both free and encapsulated islets in 20, 40, 60 μm and 40 nm NanoGlands. (C) NanoGlands (20, 40, and 60 μm) loaded with human islets were cultured for 30 days. Stimulation index of insulin release was measured at day 5 and 27, and reported for all the groups as means ± SE. (D) Optical imagine of human islets encapsulated in 40 μm NanoGland stained for insulin at day 30 post-encapsulation. (E–F) confocal imaging with 3D z-stack reconstruction of islets stained for insulin and retrieved from a 60 μm NanoGland, at day 30.
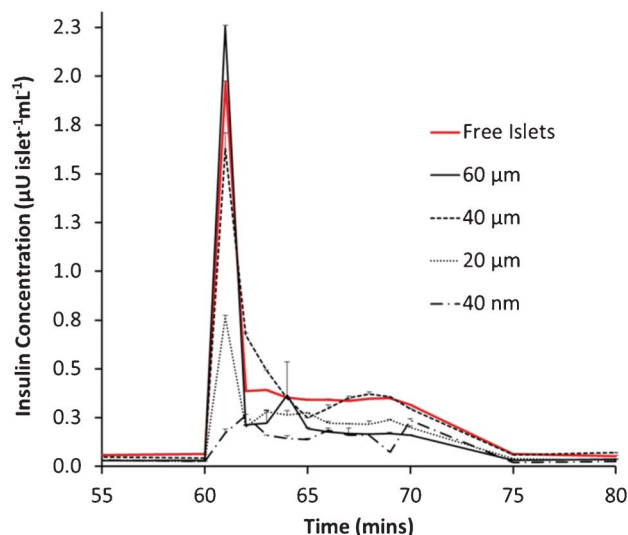
Fig. 7 Perifusion experiment: Dynamic insulin release profile for the 40 nm, 20, 40, 60 μm and free human islets.

In summary, the *in vitro* data validated the mathematical model by qualitatively correlating with the predicted glucose and insulin diffusion through 20, 40 and 60 μm and 40 nm membranes (Fig. 5B). Additionally, human islets encapsulated in the NanoGland for 30 days in culture were shown to be capable of preserving their insulin storage (Fig. 6D–F), and responsiveness to glucose challenge (Fig. 6C).

Islet retention in NanoGlands

The size distribution of the islets was obtained by analyzing 30 optical images of human islet samples, independently collected. A representative islet image is shown in ESI† Fig. S6. Over 900 islets were sized and measured with imaging software and plotted in Fig. 8A. The islet distribution shows a characteristic positive-skewed Gaussian profile ($\gamma = 1.4$) with sizes ranging from 25 to 500 μm and a population peak around 100–150 μm, which correlates with previously reported data.[19]

The retention of islets in the NanoGlands presenting different channel sizes (200, 60, 40 and 20 μm) was tested *in vitro* employing the insert-well set up (Fig. 4A), as previously described. Each islet aliquot (150–500 IEQ) was characterized in terms of number and size before loading into baskets. After 24 h of incubation under gentile agitation, the number of islets lost through the channels and accumulated in the well plate were counted and sized. The size distributions of the islets loaded and lost from each type of membrane are reported in Fig. 8B–E.

As expected, large channels (200 μm, comparable in size to macro-pores in scaffolds) led to a greater loss of islets ranging in size from <50 to 200 μm (Fig. 8B). Smaller channels (60, 40, and 20 μm) improved islet retention by 70 to 83% (Fig. 8C–E). It has to be noted that islet rupture may have occurred during the experiment due to their delicate structure. This can explain, the larger number of islets lost with respect to islets loaded as shown in Fig. 8B–E for the size group <50 μm. Small islet aggregation, instead, explains the detection of a few 50–100 μm islets among those ones lost from 20 μm membranes (Fig. 8E). According to their size distribution, 71% of islets are <200 μm, therefore smaller channel/pore devices could
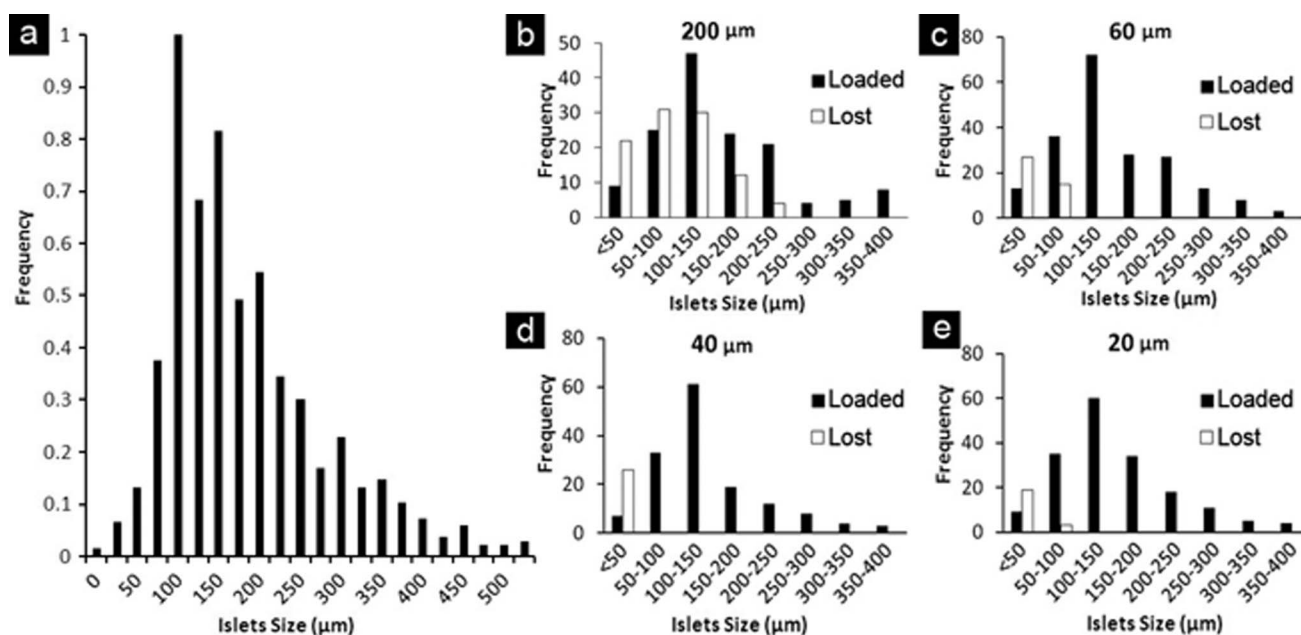

Fig. 8 NanoGland islets retention *in vitro*. A) Dithizone (DTZ) stained-human islets size distribution, B–E) Size distribution of islets loaded (black) and lost (white) from NanoGlands possessing different channel sizes.
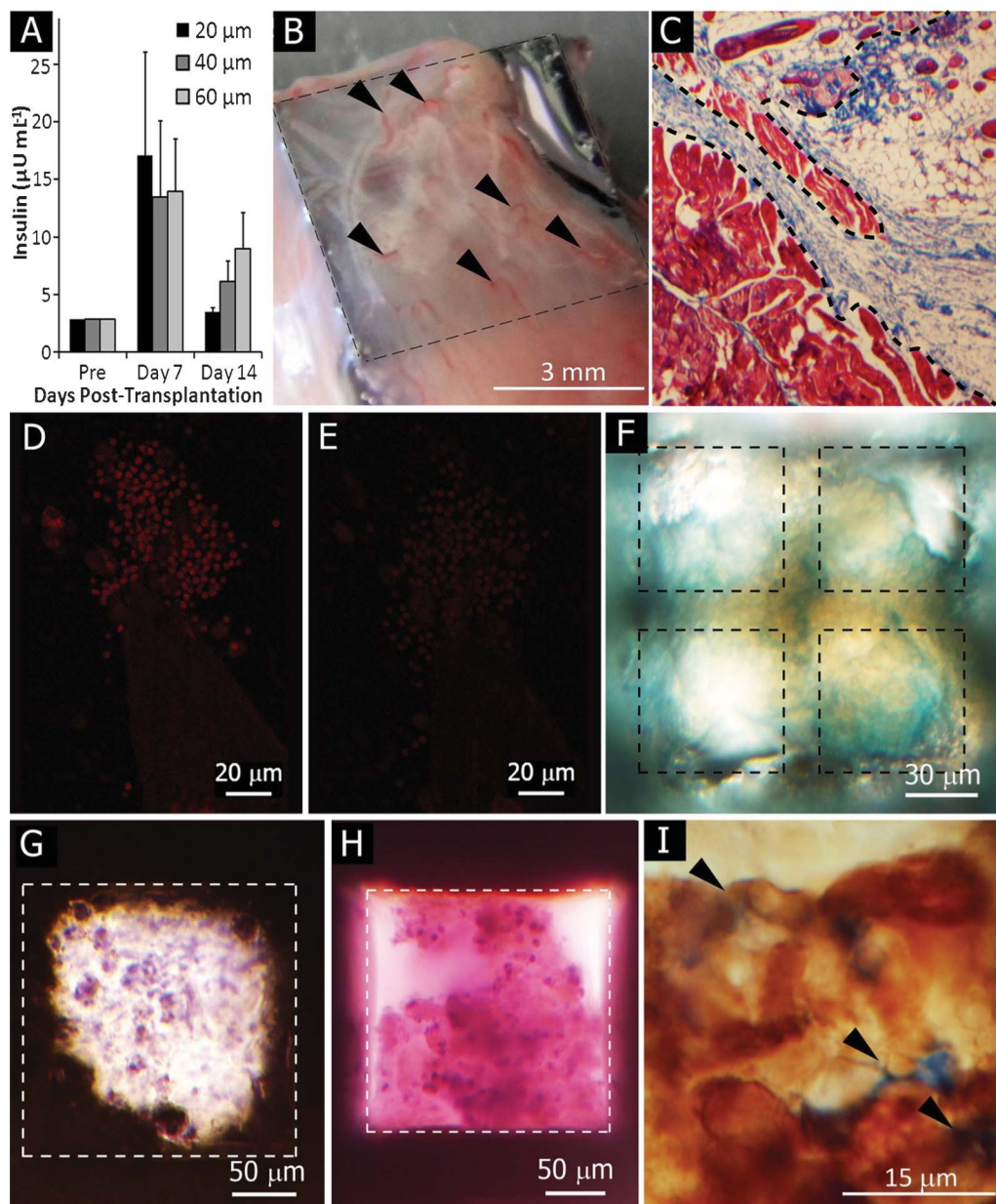
Fig. 9 *In vivo* testing: Aliquots of human islets (1000 IEQ) were transplanted free under the left kidney capsule of nude mice or loaded into 20, 40, or 60 μm NanoGlands and implanted subcutaneously in the animals' dorsum (*n* = 5 mice/group, 3 NanoGlands/mouse). At 120 days post-transplantation tissues surrounding 60 μm NanoGlands were harvested and islets retrieved for further analysis. (A) Human insulin levels (presented as mean ± SE) were measured 30 mins post-glucose challenge at day 0 (pre-transplant), day 7 and 14 post-transplant. (B) Optical imaging of vascularized tissues surrounding a NanoGland retrieved from subcutaneous implantation in nude mice after 120 days (arrows point to vessels). (C) Histological analysis of tissues surrounding the NanoGland using Masson's Trichrome staining for collagen (blue, fibrotic area demarcated with dot line). (D–F) Confocal analysis of human islets: (D) insulin staining and (E) negative control. (F) Histological analysis of human islets staining for insulin (blue) and glucagon (brown). (G) TUNEL staining (viable cells in purple, apoptotic cells in brown). (H–I) Analysis of infiltrated mouse endothelial cells staining for CD-31 (H, in brown) and CD-34 (I, in blue) markers.

potentially lead to significant improvement in islet retention and maximize transplantation efficiency.

The optimal NanoGland architecture results from a compromise between rapid molecule exchange, including glucose and insulin, islet viability and retention. In this context, both theoretical model and *in vitro* data suggest that 60 and 40 μm NanoGlands provide favorable diffusion profiles while minimizing islet loss, and therefore represent the most promising candidates for *in vivo* testing.

In vivo viability and vascularization of NanoGland-transplanted islets

30 days assessment of human islet function *in vivo*

Aliquots of human islets (1000 IEQ) were transplanted into non-diabetic nude mice either free under the left kidney capsule or loaded in 20, 40, or 60 μm NanoGlands subcutaneously (20 animals total including control animals, *n* = 5

mice/group, 3 NanoGlands per mouse). Human insulin levels were measured 30 mins post-intraperitoneal glucose challenge, at day 0 (pre-transplant), day 7 and 14 post-transplant (Fig. 9A). Although the overall insulin levels in NanoGland transplanted animals were lower than the levels produced by free human islets transplanted under the kidney capsule (ESI† Fig. S7), human islets were responsive to the glucose challenge with insulin levels above 5.0 μU mL^{-1} (the established cutoff for determination of islet function).

The disparity observed between the free human islets and the encapsulated islets is a result of potential differences in metabolic activity, diffusion rate of glucose and insulin through the NanoGlands, and the different implantation site (kidney capsule *vs.* subcutaneous).

The inherent environment of the transplantation site is strongly correlated to islet engraftment outcomes. An ideal site would be one that provides an intimate vascular supply for adequate oxygenation, real-time access to blood glucose levels, mechanical protection of the implant, minimal inflammation, and ease in access and retrievability. The subcutaneous site is particularly appealing given its accessibility; however, low vascular access and high mechanical stress commonly result in poor engraftment of islets.[42,43] These environmental conditions are likely to have contributed to the decrease in insulin production from day 7 to day 14. Cell death is unlikely a major contributor to the disparity at 30 days since the TUNEL assay (see below) demonstrated the islets' viability for 120 days post-transplantation. In future studies, pre-vascularization of the site will be performed to promote rapid islet engraftment.

120 day endothelial infiltration study

Human islets were loaded into 20, 40, and 60 μm NanoGlands (approximately 350 IEQ/NanoGland) and subcutaneously implanted in non-diabetic nude mice. At day 120, human insulin was measured at 30 and 90 mins post-glucose challenge. Insulin levels were low (0.64 and 0.69 μU mL^{-1} for 60 and 20 μm NanoGlands, respectively), however they were detectable, suggesting that the function of the islets was preserved. The optical microscopy and histological analysis performed on tissues surrounding the NanoGlands showed the presence of vessels (Fig. 9B), and typical signs of fibrosis as the body's reaction toward the implanted device (Fig. 9C, collagen staining in blue). NanoGlands were opened and loaded human islets were stained for insulin (Fig. 9D and E and ESI† Fig. S9, in red; and Fig. 9F, in blue) and glucagon (Fig. 9F, in brown) to confirm that both β and α cells were functional. Tunnel staining (Fig. 9G) was employed to assess the islets' viability. Both assays were qualitatively positive supporting viability and preservation of the islets' function after 120 days subcutaneous implantation. In addition, mouse endothelial cell markers CD31 and CD34 (Fig. 9H, in dark brown; and Fig. 9I and ESI† Fig. S8, in blue, respectively) were used to investigate endothelial cell infiltration within the islets through the NanoGlands. Both markers revealed the presence of mouse endothelial cells suggesting signs of revascularization of the transplanted tissues. These *in vivo* results are in line with the prediction of the mathematical model and with previous studies reported in the literature showing micro-

channel guided vessel formation.[41] The selected NanoGlands (20, 40, and 60 μm) indeed allowed for insulin release *in vivo*, providing a suitable environment for islet viability over 120 days as well as endothelial cell infiltration, all of which are fundamental requisites for a successful transplantation.

Conclusions

In this work, we have developed and validated a novel silicon-based encapsulation architecture, the NanoGland, for the transplantation of human pancreatic islets. The NanoGland structure was designed to provide the graft with a physiological-like environment while minimizing islet loss, as well as providing agile access to the transplanted islets, in view of clinical applications. A mathematical model of the NanoGland was developed to predict the glucose stimulated response from encapsulated islets and to rationally optimize the device architecture. Given their higher response to glucose stimuli as compared to nanochannel membranes, microchannel NanoGlands were deemed to be most relevant for further testing. The *in vitro* experimental results with both a static and a perifusion testing performed with NanoGlands were in good agreement with the theoretical findings. More importantly, *static* results confirmed the ability of islets to secrete insulin in response to glucose challenge after 30 days in culture, maintaining a stimulation index larger than 1. Further, NanoGlands possessing 20 to 60 μm microchannels were found to dramatically increase islets retention (70 to 80%) as compared to 200 μm-channeled membranes, which, in our study, mimic the pore size of the scaffolds under investigation for islet transplantation. *In vivo* results of human islets subcutaneously transplanted within 60 and 40 μm NanoGlands in nude mice showed islet viability and responsiveness for up to 120 days post-transplantation. Finally, graft neovascularization was observed based on the presence of infiltrated mouse endothelial cells into islets retrieved from the transplanted NanoGland.

This study provides a proof of concept for a novel and promising approach for pancreatic islet transplantation, which minimizes islet loss while allowing for islet viability, responsiveness to glucose stimuli and endothelial cell infiltration. Further work is needed to optimize the NanoGland, including the adoption of biodegradable materials to provide the islets with growth factors and oxygen in support of their viability during graft revascularization, and to enhance fluid transport through the encapsulation.

Acknowledgements

provided by the Integrated Islet Distribution Program (City of Hope, Duarte CA).

References

1 F. Bertuzzi, S. Marzorati and A. Secchi, *Curr. Mol. Med.*, 2006, **6**, 369–374 http://www.ncbi.nlm.nih.gov/pubmed/16900660.

2 A. M. J. Shapiro, C. Ricordi, B. J. Hering, H. Auchincloss, R. Lindblad, R. P. Robertson, A. Secchi, M. D. Brendel, T. Berney, D. C. Brennan, E. Cagliero, R. Alejandro, E. A. Ryan, B. DiMercurio, P. Morel, K. S. Polonsky, J.-A. Reems, R. G. Bretzel, F. Bertuzzi, T. Froud, R. Kandaswamy, D. E. R. Sutherland, G. Eisenbarth, M. Segal, J. Preiksaitis, G. S. Korbutt, F. B. Barton, L. Viviano, V. Seyfert-Margolis, J. Bluestone and J. R. T. Lakey, *N. Engl. J. Med.*, 2006, **355**, 1318–1330, DOI: 10.1056/NEJMoa061267.

3 C. Chen, R. Moreno, B. Samikannu, R. G. Bretzel, M. L. Schmitz and T. Linn, *American Journal of Transplantation*, 2011, **11**, 215–224, DOI: 10.1111/j.1600-6143.2010.03390.x.

4 K. Ishiyama, J. Rawson, K. Omori and Y. Mullen, *Transplantation*, 2011, **91**, 952–960, DOI: 10.1097/TP.0b013e3182139dc1.

5 J. Henriksnas, J. Lau, G. Zang, P. O. Berggren, M. Kohler and P. O. Carlsson, *Diabetes*, 2012, **61**, 665–673, DOI: 10.2337/db10-0895.

6 A. Lukinius, L. Jansson and O. Korsgren, *The American journal of pathology*, 1995, **146**, 429–435 http://www.ncbi.nlm.nih.gov/pubmed/7531955.

7 O. M. Sabek, D. W. Fraga, O. Minoru, J. L. McClaren and A. O. Gaber, *Transplant. Proc.*, 2005, **37**, 3415–3416, DOI: 10.1016/j.transproceed.2005.09.049.

8 O. M. Sabek, D. R. Marshall, O. Minoru, D. W. Fraga and A. O. Gaber, *Transplant. Proc.*, 2005, **37**, 3441–3443, DOI: 10.1016/j.transproceed.2005.09.054.

9 O. M. Sabek, D. R. Marshall, R. Penmetsa, O. Scarborough and A. O. Gaber, *Transplant. Proc.*, 2006, **38**, 3678–3679, DOI: 10.1016/j.transproceed.2006.10.117.

10 E. Pedraza, A. C. Brady, C. A. Fraker, R. D. Molano, S. Sukert, D. M. Berman, N. S. Kenyon, A. Pileggi, C. Ricordi and C. L. Stabler, *Cell Transplant.*, 2012, 1123–1135, DOI: 10.3727/096368912X657440.

11 D. M. Salvay, C. B. Rives, X. Zhang, F. Chen, D. B. Kaufman, W. L. Lowe Jr. and L. D. Shea, *Transplantation*, 2008, **85**, 1456–1464, DOI: 10.1097/TP.0b013e31816fc0ea.

12 R. F. Gibly, X. Zhang, W. L. Lowe and L. D. Shea, *Cell transplantation*, 2012, DOI: 10.3727/096368912X636966.

13 N. E. Davis, L. N. Beenken-Rothkopf, A. Mirsoian, N. Kojic, D. L. Kaplan, A. E. Barron and M. J. Fontaine, *Biomaterials*, 2012, **33**, 6691–6697, DOI: 10.1016/j.biomaterials.2012.06.015.

14 R. B. Jalili, A. Moeen Rezakhanlou, A. Hosseini-Tabatabaei, Z. Ao, G. L. Warnock and A. Ghahary, *J. Cell. Physiol.*, 2011, **226**, 1813–1819, DOI: 10.1002/jcp.22515.

15 Y. Kawakami, H. Iwata, Y. J. Gu, M. Miyamoto, Y. Murakami, A. N. Balamurugan, M. Imamura and K. Inoue, *Pancreas*, 2001, **23**, 375–381 http://www.ncbi.nlm.nih.gov/pubmed/11668206.

16 M. Perez-Basterrechea, R. M. Briones, M. Alvarez-Viejo, E. Garcia-Perez, M. M. Esteban, V. Garcia, A. J. Obaya, L. Barneo, A. Meana and J. Otero, *Tissue Eng. A*, 2009, **15**, 569–577, DOI: 10.1089/ten.tea.2008.0088.

17 J. T. Daoud, M. S. Petropavlovskaia, J. M. Patapas, C. E. Degrandpre, R. W. DiRaddo, L. Rosenberg and M. Tabrizian, *Biomaterials*, 2011, **32**, 1536–1542, DOI: 10.1016/j.biomaterials.2010.10.036.

18 H. Blomeier, X. Zhang, C. Rives, M. Brissova, E. Hughes, M. Baker, A. C. Powers, D. B. Kaufman, L. D. Shea and W. L. Lowe Jr., *Transplantation*, 2006, **82**, 452–459, DOI: 10.1097/01.tp.0000231708.19937.21.

19 R. Lehmann, R. A. Zuellig, P. Kugelmeier, P. B. Baenninger, W. Moritz, A. Perren, P. A. Clavien, M. Weber and G. A. Spinas, *Diabetes*, 2007, **56**, 594–603, DOI: 10.2337/Db06-0779.

20 T. A. Desai, W. H. Chu, J. K. Tu, G. M. Beattie, A. Hayek and M. Ferrari, *Biotechnol. Bioeng.*, 1998, **57**, 118–120 http://www.ncbi.nlm.nih.gov/pubmed/10099185.

21 C. Smith, R. Kirk, T. West, M. Bratzel, M. Cohen, F. Martin, A. Boiarski and A. A. Rampersaud, *Diabetes Technol. Ther.*, 2005, **7**, 151–162, DOI: 10.1089/dia.2005.7.151.

22 T. A. Desai, W. H. Chu, J. K. Tu, P. Shrewsbury and M. Ferrari, *Proc. SPIE*, 1997, 216–226, DOI: 10.1117/12.269972.

23 T. A. Desai, W. H. Chu, M. Ferrari, G. Rasi, P. Sinibaldi-Vallebona, P. Borboni, G. Beattie and A. Hayek, *Proc. SPIE*, 1998, 40–47, DOI: 10.1117/12.304387.

24 D. Fine, A. Grattoni, S. Hosali, A. Ziemys, E. De Rosa, J. Gill, R. Medema, L. Hudson, M. Kojic, M. Milosevic, L. Brousseau Iii, R. Goodall, M. Ferrari and X. Liu, *Lab Chip*, 2010, **10**, 3074–3083, DOI: 10.1039/c0lc00013b.

25 A. Grattoni, J. Gill, E. Zabre, D. Fine, F. Hussain and M. Ferrari, *Anal. Chem.*, 2011, **83**, 3096–3103, DOI: 10.1021/ac1033648.

26 W. M. Deen, *AIChE J.*, 1987, **33**, 1409–1425, DOI: 10.1002/aic.690330902.

27 S. G. Schultz and A. K. Solomon, Determination of the Effective Hydrodynamic Radii of Small Molecules by Viscometry, *J. Gen. Physiol.*, 1961, 1189–1199.

28 O. Hosoya, S. Chono, Y. Saso, K. Juni, K. Morimoto and T. Seki, *J. Pharm. Pharmacol.*, 2004, **56**, 1501–1507, DOI: 10.1211/0022357044878.

29 M. Dathe, K. Gast, D. Zirwer, H. Welfle and B. Mehlis, *Int. J. Pept. Protein Res.*, 1990, **36**, 344–349 http://www.ncbi.nlm.nih.gov/pubmed/2079389.

30 A. Ziemys, M. Kojic, M. Milosevic, N. Kojic, F. Hussain, M. Ferrari and A. Grattoni, *J. Comput. Phys.*, 2011, **230**, 5722–5731, DOI: 10.1016/j.jcp.2011.03.054.

31 E. Lauga and H. A. Stone, *J. Fluid Mech.*, 2003, **489**, 55–77, DOI: 10.1017/S0022112003004695.

32 D. E. Harrison, M. R. Christie and D. W. Gray, *Diabetologia*, 1985, **28**, 99–103 http://www.ncbi.nlm.nih.gov/pubmed/3884420.

33 I. J. Stamper and X. Wang, *J. Theor. Biol.*, 2013, **318**, 210–225, DOI: 10.1016/j.jtbi.2012.11.002.

34 B. T. Rush, D. W. Fraga, M. Y. Kotb, O. M. Sabek, A. Lo, L. W. Gaber, A. B. Halim and A. O. Gaber, *Transplantation*, 2004, **77**, 1147–1154 http://www.ncbi.nlm.nih.gov/pubmed/15114076.

35 D. W. Fraga, O. Sabek, D. K. Hathaway and A. O. Gaber, *Transplantation*, 1998, **65**, 1060–1066 http://www.ncbi.nlm.nih.gov/pubmed/9583866.

36 A. Osama Gaber, A. Chamsuddin, D. Fraga, J. Fisher and A. Lo, *Transplantation*, 2004, **77**, 309–311, DOI: 10.1097/01.TP.0000101509.35249.A0.

37 D. W. Fraga, A. O. Gaber and M. Kotb, *Methods in molecular medicine*, 2005, **107**, 303–311 http://www.ncbi.nlm.nih.gov/pubmed/15492381.

38 S. Liu, T. Okada, A. Assmann, J. Soto, C. W. Liew, H. Bugger, O. S. Shirihai, E. D. Abel and R. N. Kulkarni, *PLoS One*, 2009, **4**, e7983, DOI: 10.1371/journal.pone.0007983.

39 E. W. Kraegen, L. Lazarus and L. V. Campbell, *Metab., Clin. Exp.*, 1983, **32**, 622–627 http://www.ncbi.nlm.nih.gov/pubmed/6341777.

40 W. K. Waldhausl, S. Gasic, P. Bratusch-Marrain, A. Korn and P. Nowotny, *The American journal of physiology*, 1982, **243**, E476–482 http://www.ncbi.nlm.nih.gov/pubmed/6756164.

41 C. Anderwald, A. Tura, A. Grassi, M. Krebs, J. Szendroedi, M. Roden, M. G. Bischof, A. Luger and G. Pacini, *Diabetes Care*, 2011, **34**, 437–441, DOI: 10.2337/dc10-1137.

42 J. H. Juang, S. Bonner-Weir, Y. Ogawa, J. P. Vacanti and G. C. Weir, *Transplantation*, 1996, **61**, 1557–1561 http://www.ncbi.nlm.nih.gov/pubmed/8669096.

43 J. H. Juang, B. R. S. Hsu and C. H. Kuo, *Transplant. Proc.*, 2005, **37**, 3479–3481 http://dx.doi.org/10.1016/j.transproceed.2005.09.023.